Southeast Indian Ocean-Ridge earthquake sequences from cross-correlation analysis of hydroacoustic data

Sukyoung Yun,[1,2] Sidao Ni,[3] Minkyu Park[2]* and Won Sang Lee[2]

[1]*SEES, Seoul National University, Seoul, Korea*
[2]*Korea Polar Research Institute, Incheon, Korea. E-mail: minkyu@kopri.re.kr*
[3]*Mengcheng National Geophysical Observatory, University of Science and Technology of China, Hefei, Anhui, China*

SUMMARY

Parameters of earthquake sequences, for instance location and timing of foreshocks and after-shocks, are critical for understanding dynamics of mid-ocean ridge and transform faults. Whole sequences including small earthquakes in the ocean cannot be well recorded by land-based seismometers due to large epicentral distances. Recent hydroacoustic studies have demonstrated that T waves are very effective in detecting small submarine earthquakes because of little energy loss during propagation in Sound Fixing and Ranging channel. For example, an $M_W 6.2$ (2006 March 6, 40.11°S/78.49°E) transform-fault earthquake occurred at the Southeastern Indian Ocean Ridge, but National Earthquake Information Center only reported three aftershocks in the first following week. We applied cross-correlation method to hydroacoustic data from the International Monitoring System arrays in the Indian Ocean to examine the whole earthquake sequence. We detected 14 aftershocks and none foreshock for the earthquake and locations of these aftershocks show an irregular pattern. From the observation, we suggest that the feature could be caused by complicated transcurrent plate-boundary dynamics between two overlapped spreading ridges that is possibly explained by the bookshelf faulting model.

Key words: Seismicity and tectonics; Guided waves; Indian Ocean.

GJI Seismology

INTRODUCTION

Seismological studies such as source mechanism, locations and rupture velocity, have provided important information about geodynamic processes, especially mid-ocean ridge (MOR) process. For instance, earthquake swarms are sometimes associated with dike propagation/intrusion. Investigations of source mechanism and location of a series of earthquake sequence enable us to understand which fault plane the rupture occurs on, and the extent of the rupture process.

Marine geophysicists have used many submarine earthquake data to figure out dynamics of MOR systems (e.g. Dziak *et al.* 1995; Fox *et al.* 2001; Smith *et al.* 2002). However, submarine small earthquakes ($M_W < 4$) are quite difficult to detect using land-based seismic networks. In many cases, it is even harder to locate them accurately because of poor azimuthal coverage of seismic stations and low signal-to-noise ratio. Even though installation of Ocean Bottom Seismometer (OBS) can improve detection capability of small events in the ocean, the expense and limited temporal and spatial availability is an obstacle to most OBS experiments for global tectonic studies. In 1990s, NOAA scientists developed Autonomous Underwater Hydrophones and have monitored micro-

earthquakes in the ocean. The hydroacoustic method turns out to be a very efficient tool to study submarine tectonic activities in detail (Dziak *et al.* 1995; Dziak & Fox 1999; Fox *et al.* 2001; Bohnenstiehl *et al.* 2004). The higher detection capability comes from the propagation efficiency of T waves in the SOund Fixing And Ranging (SOFAR) channel (Tolstoy & Ewing 1950). T waves are seismically generated acoustic waves that are trapped and propagate within the SOFAR channel. These acoustic guided waves have some different characteristics compared to seismic waves. First, T waves can travel very far and contain high frequency energy because the transmission loss is much less than that of the seismic waves as well as because water column is much more homogeneous than the solid Earth. Second, the sound velocity profile of ocean is significantly well defined and the propagating velocity is very low (1.45–1.5 km s^{-1}) compared to seismic P and S waves. These characteristics of T wave provide an ideal way to observe and determine the location of micro-earthquakes in the ocean.

Indeed, hydroacoustic studies have greatly improved our understanding of tectonics in the Pacific and Atlantic oceans (e.g. Dziak *et al.* 1995; Smith *et al.* 2002; Bohnenstiehl & Tolstoy 2003) using the NOAA hydrophone arrays. To date, tectonic studies in the Indian Ocean are fairly limited (Bohnenstiehl *et al.* 2004; Graeber & Piserchia 2004; Hanson & Bowmen 2005). The Southeast Indian Ocean Ridge (SEIR), an intermediate spreading ridge with 58–76 mm yr^{-1} (Sempere & Klein 1995), shows a lot of complexities in

*Corresponding author.
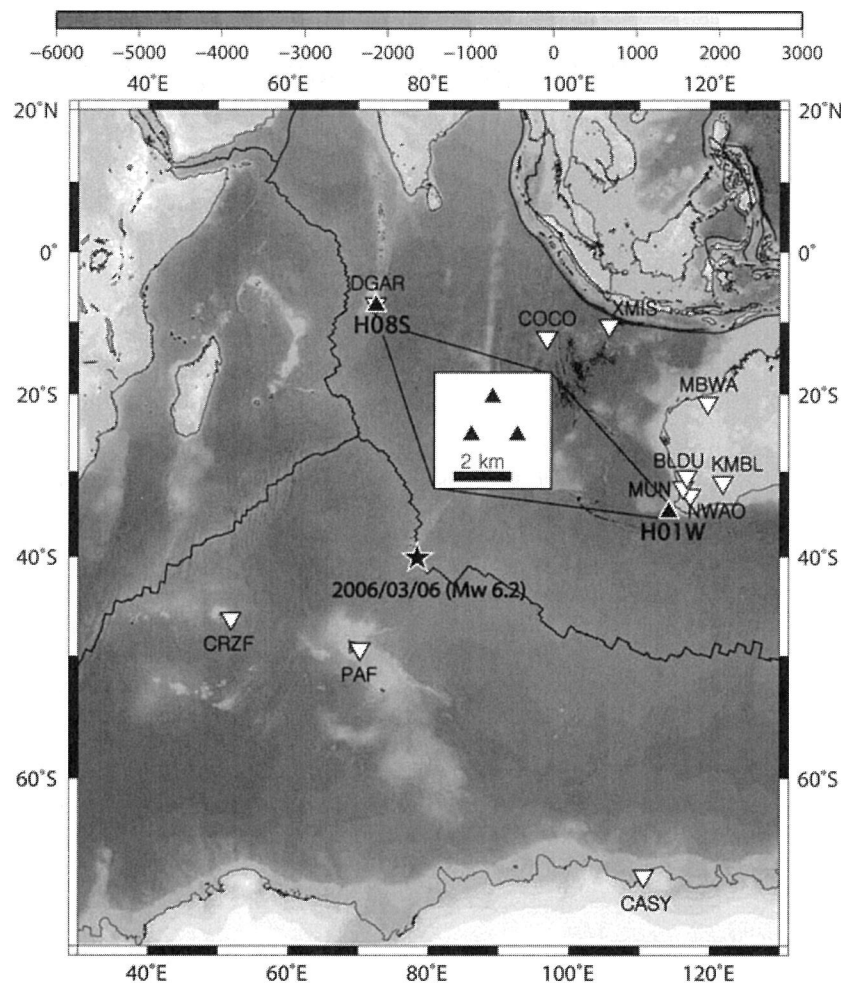
Figure 1. Bathymetric map of the Indian Ocean. The black solid line represents plate boundary, and the star denotes M_W 6 .2 (2006 March 6, 40.11°S/78.49°E) transform-fault earthquake. The triangles are IMS hydrophone triplet stations, H01W array at CL (centre on the map) and H08S array at SDG (right on the map). The inverse triangles are the Global Seismographic Network (GSN) stations used for Rayleigh-wave cross-correlation analysis. Boundary information is from Bird (2003).

tectonic evolution. In particular, its transform fault systems are not well defined on the Amsterdam-St. Paul hotspot platform near the SEIR (Scheirer *et al.* 2000). Therefore, accurate patterns of seismicity are useful to provide insight into the complicated tectonic evolution. We chose a typical transform fault earthquake (2006 March 6, 40.11°S/78.49°E, $M_W6.2$) that occurred at the SEIR to relocate the event (Fig. 1) and its aftershock sequence using hydroacoustic data to investigate detailed seismicity along the complicated transform fault system.

DATA

The SEIR is quite seismically active with many $M_W \geq 6$ earthquakes in the past 30 yr (Fig. 2). Most of the strong earthquakes ($M_W \geq 6$) have almost pure strike slip source mechanism and delineate along transform faults well, whereas smaller events (grey dots in Fig. 2) show much scattered distribution that could be either caused by mislocation of events or complicated evolution of transform fault system.

International Monitoring System (IMS) hydrophone stations are designed to detect acoustic signals from the underwater explosions, and they are maintained by Comprehensive Nuclear-Test-Ban Treaty Organization (CTBTO). There are three hydroacoustic arrays in the Indian Ocean including the H01W array at Cape Leeuwin (CL) and H08S array at South Diego Garcia (SDG) (Fig. 1). Each individual array consists of three hydrophones and their distances between each other are about 2 km. Each instrument has a pressure sensor with almost flat response within 3 dB over the frequency band 2–20 Hz, and a 24 bit digitizer. Its sampling rate is 250 Hz. We used continuous hydroacoustic data recorded between 2006 March 3 22:20:00 and 2006 March 10 18:20:00 that include the whole sequence associated with the earthquake (2006 March 6, 40.11°S/78.49°E, $M_W6.2$). We choose 3 days of data before the mainshock to investigate whether foreshock occurred because foreshock may be associated with slow slip of transform faults (McGuire *et al.* 2003), and 4 days of data to investigate immediate aftershocks that are informative for understanding rupture dimension of the mainshock. Our purpose is not to cover all the aftershocks because later
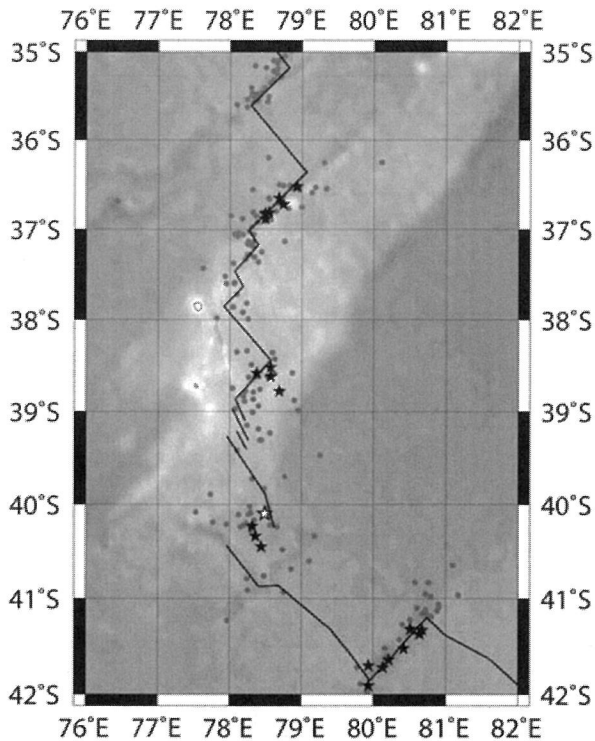
Figure 2. Seismicity reported by NEIC from 1973 February 6 to 2006 August 28 in the study area. Stars are earthquakes bigger than M_W 6, and the open star is the main event of this study. Boundaries are modified after Hanson & Bowman (2006).

aftershocks may migrate outside of rupture area of the mainshock (Tajima & Kanamori 1985).

DATA PROCESSING USING PMCC METHOD

Triangulation method has been successfully used to locate the events for the East Pacific Rise (EPR), Mid-Atlantic Ridge and Juan de Fuca ridge (Dziak *et al.* 1995; Fox *et al.* 1995; Fox *et al.* 2001; Bohnenstiehl & Tolstoy 2003). Typically, even very small events ($M \sim 1.5$) within an array could be detected by hydrophones (Dziak *et al.* 1995), however the accuracy and detection capability become poor as epicentral distance for events outside the array increases. For events far from the arrays of smaller aperture, Progressive Multi-Channel Correlation (PMCC) (Cansi 1995) has been used to process hydroacoustic data recorded on IMS hydrophones (Graeber & Piserchia 2004; Hanson & Bowman 2005). The basic concept of this method is that we can determine the wave vectors, that is speed and azimuth, by calculating traveltime differences using the cross-correlation method. This method is based upon the assumption that the wavefront is a plane in the far field. For the conditions of frequency range 2–20 Hz and average sound velocity 1.5 km s^{-1}, *T*-waves epicentral distances bigger than 53 km can be considered as the local plane wave within the range of the IMS array aperture. If signals recorded by all the three sensors are from the same source, summation of time differences between all three pairs should be very close to zero, which is called the closure condition (Graeber & Piserchia 2004). If the signals are coherent, all the three correlation

coefficients should be close to 1. To efficiently and reliably find *T*-wave signal, we impose the following criteria: (1) For coherency between signals, product of the three coefficients (PCCC) must be larger than 0.064, that is $c_{12} \times c_{23} \times c_{31} \geq (0.4)^3$, where c_{ij} is the cross-correlation coefficient between waveforms of *i*th and *j*th sensors. (2) For the closure condition, we require that $-0.016 \leq t_{12} + t_{23} + t_{31} \leq 0.016$, where t_{ij} is the traveltime difference of signals between *i*th and *j*th sensors calculated from cross-correlation. We also need a velocity criterion that the speed value of a wave vector, v_t, has to be 1.45–1.5 km s^{-1}. (3) Because we are only concerned with the earthquake sequence in the study region, we also limit estimated backazimuth to be within range of the backazimuth of the main event $\pm 1°$ (64×55 km).

We performed cross-correlation on the signals in the 2–20 Hz frequency band with a moving time window of 3.2 s. This frequency band is chosen because teleseismic hydroacoustic signals are band-limited between 2 and 8 Hz (Hanson & Bowman 2005), and intensity for a frequency of 20 Hz at a receiver of 4000 km is not negligible (de Groot-Hedlin & Orcutt 2001). Fig. 3 shows an example of hydrophone triad (H01W) data and depicts results from cross-correlation analysis. Figs 3(e)–(g) are time series of the event signals recorded at the three sensors of CL station at 2006 March 6 20:48:20, and Fig. 3(h) is a spectrogram of Fig. 3(e). Fig. 3(a) is the sum of three relative time differences, and Fig. 3(b) is PCCC. Figs 3(c) and (d) are speed and backazimuth values of the wave vector calculated from the time differences.

RESULTS

We detected 14 aftershocks of the main event, but did not find any foreshocks. Fig. 4 shows an example of PMCC result for 10,000 s. The pink and blue boxes indicate the mainshock and aftershocks, respectively. The events signals arrive at CL station around 320 s earlier than at SDG station. The correlated event signals in CL station are usually longer and the PCCC are smaller than those of SDG station. For example the fifth aftershock, the last event in Fig. 4, the correlated signal durations are 84 and 31 s, the averaged coherency values are 0.148 and 0.221 in CL and SDG station, respectively. This may indicate that propagation to CL is more disturbed than SDG. We estimated backazimuth from the highest PCCC point within the cross-correlation window including the peak amplitude point, and they are used to locate each event obtained under the criteria because the strongest scattering energy usually coupled into the water column around the epicentre in abyssal regions (Yang & Forsyth 2003). The backazimuth values of the main event are 171.72° at the CL and 248.82° at the SDG station.

Because accurate seismic pattern can provide very detailed information on dynamics of the tectonic boundaries, we employ the relative location method. The relative location approach has been turned out to be very effective for imaging fine scale fault structures on continents such as San Andreas Fault (Haukson & Shearer 2005) whereas absolute locating method cannot provide such accuracy yet. Because the main event signal shows broad and complicated envelope that is hard to find a peak point, we set the biggest aftershock reported at the global Centroid Moment Tensor (CMT) catalogue (2006 March 7 07:10:54.1, 40.06°S/78.26°E, M_W5.8) as a reference event instead. CMT solutions provide the hypocentral coordinates of the centroid of the stress glut density (Dziewonski *et al.* 1981). This concept agrees well with the hydroacoustic location algorithm. Then we located the aftershocks from relative azimuthal differences.
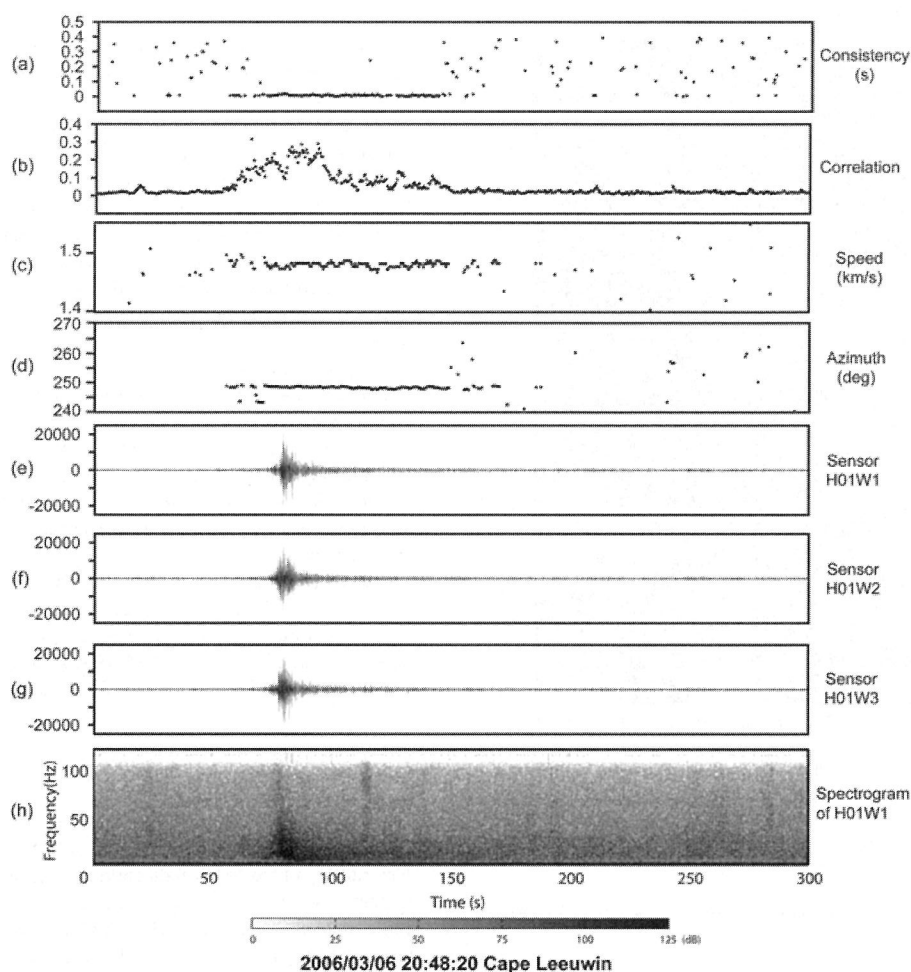
Figure 3. Example of hydrophone triad (H01W) data and cross-correlation analysis. From the top to the bottom, (a) the sum of three relative time differences, (b) products of three cross-correlation coefficients, (c) speed, (d) azimuth, (e)-(g) time series of the three triplet, and (h) spectrogram of H01W1 signal recorded in 2006 March 6 20:48:20.

Table 1 is a catalogue of the detected earthquakes, and where the 10 earthquakes among them are not reported by the National Earthquake Information Center (NEIC) and Bulletin of the International Seismological Centre Collect Data (ISCCD). Though we did not determine magnitude of most of the aftershocks, we report peak amplitude of T-waves instead that depends on magnitude, focal depth and focal mechanism (Dziak 2001). Therefore we cannot specify the detection threshold without the magnitude information, but the study of Hanson & Bowman (2005) suggests the detection threshold could be one magnitude lower than that from NEIC. The main event is followed by 14 aftershocks including the biggest one ($M_W 5.8$) until 2006 March 8 18:14:23.28. In Fig. 5, these newly detected earthquakes are plotted on a side-scan sonar imagery (Scheirer *et al.* 2000). An ellipse with dashed line is error range with 90 per cent probability in Fig. 5. This error ellipse is defined by Hanson & Bowmans's (2006) azimuthal error (standard deviation : 0.18°) that is estimated from residuals of aftershock azimuths relative to a mainshock. They mentioned that this value represents an upper bound of the azimuthal error for collocating because aftershocks do not all occur at the same place in general.

To show the spatial distribution of the aftershock sequence clearly, we compute aftershock area with 90 per cent confidence level by fitting 2-D Gaussian distribution (Kagan 2002), and the ellipse is drawn with solid line in Fig. 5. The azimuth of the major ellipse axis for the estimated aftershock area is 124°, and this is almost perpendicular to the major axis of the error ellipse. That means the elongated spatial distribution is not from error effect.

For the case of well-developed transform faults, aftershocks mostly aligned along the fault line (e.g. Bohnenstiehl *et al.* 2004). Our detected events as well as earthquakes from the NEIC catalogue are not well correlated with presumed transform faults in our study region near St. Paul island suggesting complex fault dynamics in this region (Fig. 2).

We also performed Rayleigh-wave cross-correlation analysis (McGuire 2008) to estimate the relative position between the mainshock (2006 March 6, M_W 6 .2) and the biggest aftershock (2006 March 7, $M_W 5.8$) using seismic data recorded in the 11 GSN stations (see Fig. 1). This method is simple and quite straightforward to determine relative position between two events. Fig. 6 shows
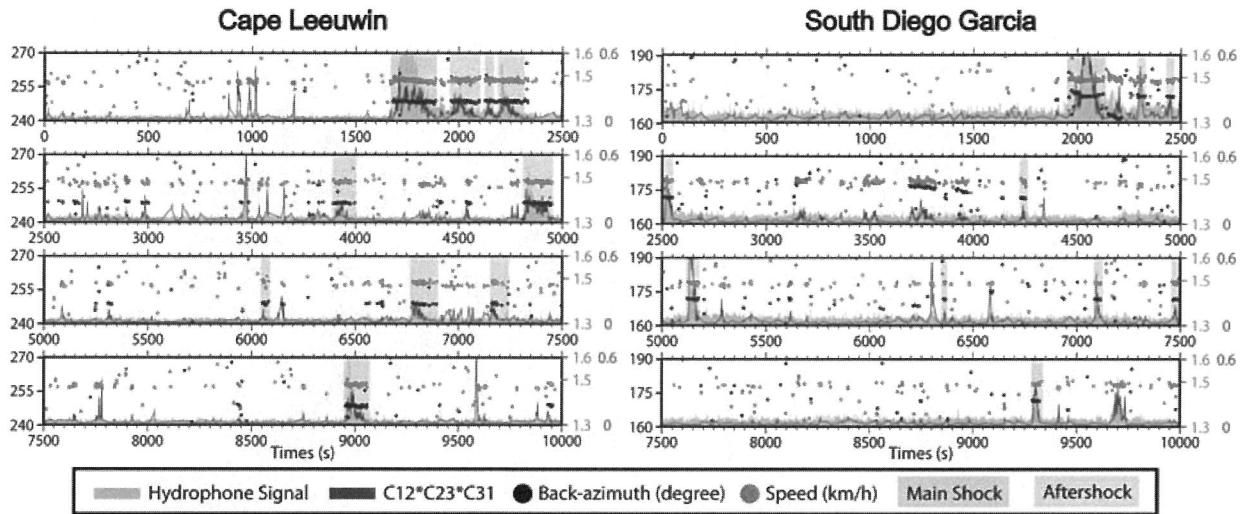
Figure 4. Plots of earthquake signal (grey line), products of three cross-correlation coefficients (green line), backazimuth (black points), speed (red points) values for the CL (left figure) and the SDG stations (right figures). The pink and blue boxes indicate the mainshock and aftershocks, respectively.

Table 1. Catalogue of the detected earthquakes, where 10 earthquakes are not listed in the NEIC and ISCCD catalogue. Locating errors are denoted as an ellipse with dashed line in Fig. 5.

Date	Time	Lat. (°S)	Lon. (°E)	M_W	Amp. (μPa)[a]	Amp. (μPa)[b]
2006 March 6	18:13:26.0	40.23	78.32	6.2	2.01E+07	2.79E+06
2006 March 6	18:50:03.3	40.24	78.41	4.0*	1.31E+06	1.50E+05
2006 March 6	19:04:57.5	40.12	78.28	4.1*	3.27E+06	5.79E+05
2006 March 6	19:25:19.2	40.23	78.30		5.80E+05	1.43E+05
2006 March 6	19:37:34.2	40.06	78.26		1.19E+06	2.61E+05
2006 March 6	19:43:50.7	40.12	78.19		1.06E+06	1.86E+05
2006 March 6	20:14:21.4	40.24	78.54		4.32E+06	2.61E+05
2006 March 7	07:10:54.1	40.06	78.26	5.8	9.19E+06	2.42E+06
2006 March 7	07:20:17.7	40.18	78.20		4.23E+05	1.44E+05
2006 March 7	07:25:44.0	40.12	78.17		3.42E+05	1.29E+05
2006 March 7	07:32:42.1	40.02	78.27		4.58E+05	1.58E+05
2006 March 7	08:49:08.6	40.13	78.17		3.88E+05	1.72E+05
2006 March 7	10:43:15.9	40.23	78.54		8.90E+05	1.16E+05
2006 March 7	19:24:22.1	40.12	78.53	4.7	3.08E+06	3.24E+05
2006 March 8	18:14:27.3	40.30	78.43		1.58E+06	1.49E+05

[a]Peak amplitude recorded at H01W1 sensor in the CL.
[b]Peak amplitude recorded at H08S1 sensor in the SDG.
*Mb from ISCCD catalogue.

that the mainshock took place 14.7 ± 5.9 km southeast (azimuth: 119 ± 18.5°) from the aftershock (reference event), which is close to the elongated direction of aftershock distribution from the PMCC result.

DISCUSSION AND CONCLUSION

Geographic patterns of strike slip fault earthquake sequences in the MOR system are mostly linear and parallel to transform faults, though some hypotheses predict that strike slip earthquakes on fault systems can occur in parallel with ridges, instead (Wetzel *et al.* 1993). Because it is not easy to decide the fault plane of strike-slip events in the MOR system, seismologists used aftershock distribution to obtain information regarding the rupture plane (Kikuchi & Kanamori 1991). Thus accurate location of aftershocks is essential for inferring a MOR system dynamics. There are two fault

planes derived from the CMT solution in Fig. 5. The strike of a fault plane (F1) is 43° (perpendicular to the MOR) and the other (F2) is 133° (comparable to the azimuth of the MOR axis). According to the Bird's plate boundary model (2002), there is a transform fault parallel to F1. However, the pattern of aftershock distribution is not aligned to the transform fault. According to the 2-D Gaussian approximation, the aftershocks are distributed along the major ellipse axis whose azimuth is 124° (see Fig. 5), and the major axis is closer to F2 direction (Fig. 5). Based on the additional Rayleigh-wave cross-correlation analysis, the resulting azimuth is also close to the F2 direction (Fig. 6). These features suggest that our study area does not show any characteristics of well-developed transform fault. Also, the bathymetry map and the side-scan sonar image (Fig. 5) shows that the spreading centres of the studied ridge segments are overlapped and the transform fault line is not clearly presented (Scheirer *et al.* 2000). According to Macdonald's classification (2001), our studied fault region belongs to the second order
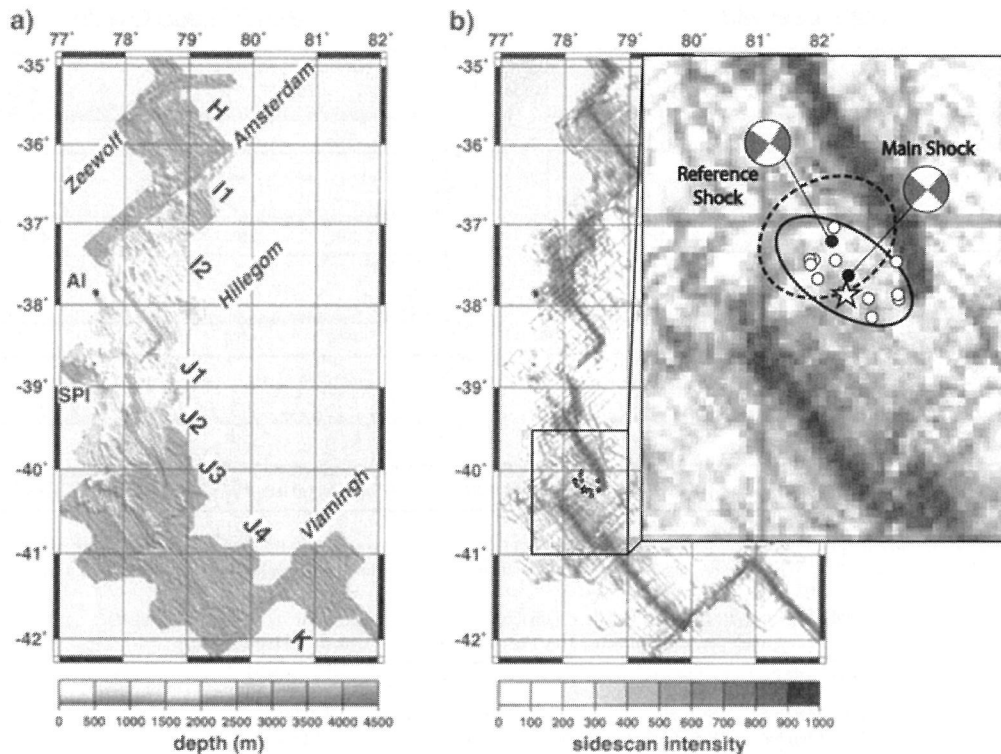
Figure 5. (a) Bathymetry map and (b) side-scan sonar image of Amsterdam-St. Paul platform and hydroacoustically detected earthquakes from this study. In the inset, black dots represent global CMT locations, and white dots and a star are the locations of the aftershocks and the mainshock determined in this study. Two-dimensional Gaussian approximation of aftershock distribution is shown as an ellipse with solid line that represents 90 per cent confidence level. An ellipse with dashed line is error range with 90 per cent probability. It is estimated by the upper bound of azimuthal error (standard deviation : 0.18°) from Hanson & Bowman (2006). In the side-scan sonar image, thick lines, the traces of lava flow, shows that the spreading centres of the studied ridge segments are overlapped and the transform fault is not well developed. The distribution of the detected events reaches to the tip of overlapped part of one ridge parallel with the other ridge (modified after *Scheirer et al.* 2000).

Overlapped Spreading Centers (OSC). Probable kinematic models for this OSC are proposed by Wetzel *et al.* (1993), and one of those models is the bookshelf fault whose rupture plane is parallel to the spreading centres. The results of the PMCC analysis and the Rayleigh-wave analysis suggest that the bookshelf fault is a possible model for the region.

Another issue is that we do not find any foreshocks for this event, which is in contrast to the case of predictive foreshocks in the EPR (McGuire *et al.* 2003). Also aftershock rates in the EPR are lower than those on continents. Because of short duration (4 days after mainshock), we cannot compare aftershocks of the SEIR mainshock with those of EPR or continents. However, if we compare aftershocks during 4 days for a M_W 6 .2 mainshock, it seems that the SEIR mainshock has much less aftershocks than continental earthquake. According to McGuire *et al.* (2003), these features are attributed to a different aftershock generation mechanism for the MOR system such as hydrothermal flow or nearby magmatic activity.

Our study shows that hydroacoustic method greatly improves efficiency of detecting and locating small submarine earthquakes, and provides a complementary tool for study of tectonic activities in MOR systems to OBS observations that can provide detailed information on source mechanisms of earthquakes. More investigations using both OBS data and hydroacoustic data are required to increase our ability to delineate dynamic process in MOR systems.

REFERENCES

Bird, P., 2003. An updated digital model of plate boundaries, *Geochem. Geophys. Geosyst.,* **4**(3), 1027, doi:10.1029/2001GC000252.

Bohnenstiehl, D. & Tolstoy, M., 2003. Comparison of teleseismically and hydroacoustically derived earthquake locations along the north-central Mid-Atlantic Ridge and Equatorial East Pacific Rise, *Seism. Res. Lett.,* **74**, 790–801.

Bohnenstiehl, D., Tolstoy, M. & Chapp, E., 2004. Breaking into the plate: a 7.6 Mw fracture-zone earthquake adjacent to the Central Indian Ridge, *Geophys. Res. Lett.,* **31**, L02615, doi:10.1029/2003GL018981.

Cansi, Y., 1995. An automatic seismic event processing for detection and location: the PMCC method, *Geophys. Res. Lett.,* **22**, 1021–1024.

de Groot-Hedlin, C.D. & Orcutt, J.A., 2001. Excitation of *T*-phase by seafloor scattering, *J. acoust. Soc. Am.,* **109**, 1944–1954.
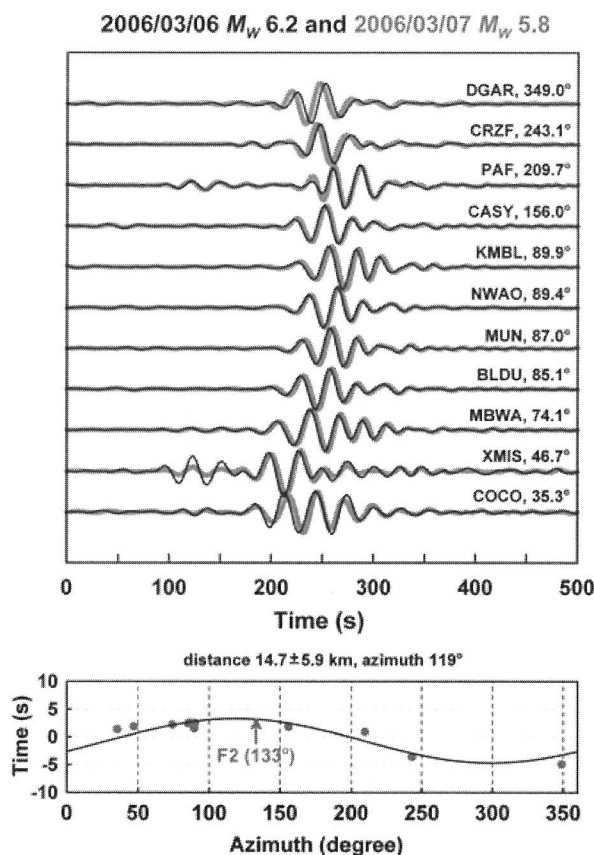
Figure 6. Measurement of the differential arrival times for Rayleigh waves applying a cross-correlation method to estimate the relative position between the mainshock (2006 March 6, M_W 6 .2) and the biggest aftershock (2006 March 7, M_W 5 .8). Seismograms are recorded in the GSN stations (Fig. 1). To determine the azimuth and the length of a line connecting those two events, we find a cosine curve (bottom panel, black line) minimizing the L1 norm for differential arrival times (bottom panel, grey dots). A grey arrow indicates the azimuth of F2, one of the possible fault plane from the CMT solution of the main event. The results represent that the main event was located 14.7 km southeast (azimuth: 119°) from the aftershock.

Dziak, R.P., Fox, C.G. & Schreiner, A.E., 1995. The June-July 1993 seismo-acoustic event at coaxial segment, Juan de Fuca Ridge: evidence for a lateral dike injection, *Geophys. Res. Lett.*, **22**, 135–138.

Dziak, R.P. & Fox, C.G., 1999. Long-term seismicity and ground deformation at axial volcano, Juan de Fuca Ridge, *Geophys. Res. Lett.*, **26**(24), 3641–3644.

Dziak, R.P., 2001. Empirical relationship of *T*-wave energy and fault parameters of northeast Pacific Ocean earthquakes, *Geophys. Res. Lett.*, **28**, 2537–2541.

Dziewonski, A.M., Chou, T.-A. & Woodhouse, J.H., 1981. Determination of earthquake source parameters from waveform data for studies of global and regional seismicity, *J. geophys. Res.*, **86**, 2825–2852.

Fox, C.G., Radford, W.E., Dziak, R.P., Lau, T.A., Matsumoto, H. & Schreiner, A.E., 1995. Acoustic detection of a seafloor spreading episode on the Juan de Fuca Ridge using military hydrophone arrays, *Geophys. Res. Lett.*, **22**(2), 131–134.

Fox, C.G., Matsumoto, H. & Lau, T.A., 2001. Monitoring Pacific Ocean seismicity from an autonomous hydrophone array, *J. geophys. Res.*, **106**, 4183–4206.

Graeber, F.M. & Piserchia, P.F., 2004. Zone of *T*-wave excitation in the NE Indian Ocean mapped using variations in back azimuth over time obtained from multi-channel correlation of IMS hydrophone triplet data, *Geophys. J. Int.*, **158**, 239–256.

Hanson, J.A. & Bowman, J.R., 2005. Indian Ocean ridge seismicity observed with a permanent hydroacoustic network, *Geophys. Res. Lett.*, **32**, L06301, doi:10.1029/2004GL021931.

Hanson, J.A. & Bowman, J.R., 2006. Methods for monitoring hydoacoustic events using direct and reflected *T* waves in the Indian Ocean, *J. geophys. Res.*, **111**, B02305, doi:10.1029/2004JB003609.

Haukson, E. & Shearer, P., 2005. Southern California hypocenter relocation with waveform cross-correlation, Part 1: results using the Double-Difference method, *Bull. seism. Soc. Am.*, **95**(3), 896–903.

Kagan, Y.Y., 2002. Aftershock zone scaling, *Bull. seism. Soc. Am.*, **92**(2), 641–655.

Kikuchi, M. & Kanamori, H., 1991. Inversion of complex body waves-III, *Bull. seism. Soc. Am.*, **81**, 2335–2350.

Macdonald, K.C., 2001. Mid-ocean ridge tectonics, volcanism and geomorphology, *Encyclopedia of Ocean Sciences*, Academic Press, pp. 1798–1813.

McGuire, J.J., Boettcher, M.S. & Jordan, T.H., 2003. Foreshock sequences and short-term earthquake predictability on East Pacific Rise transform faults, *Nature*, **434**, 457–461.

McGuire, J.J., 2008. Seismic cycles and earthquake predictability on East Pacific Rise transform faults, *Bull. seism. Soc. Am.*, **98**(3), 1067–1084.

Sempere, J.C. & Klein, E.M., 1995. New insights in crustal accretion from Indian Ocean spreading centres, *EOS, Trans. Am. geophys. Un.*, **76**, 113–116.

Scheirer, D., Forsyth, D., Conder, J., Eberle, M., Hung, S., Johnson, K. & Graham, D., 2000. Anomalous seafloor spreading of the Southeast Indian ridge near the Amsterdam–St. Paul Plateau, *J. geophys. Res.*, **105**, 8243–8262.

Smith, D.K., Tolstoy, M., Fox, C.G., Bohnenstiehl, D.R., Matsumoto, H. & Fowler, M.J., 2002. Hydroacoustic monitoring of seismicity at the slow-spreading Mid-Atlantic Ridge, *Geophys. Res. Lett.*, **29**(11), 1518, doi:10.1029/2001GL013912.

Tajima, F. & Kanamori, H., 1985. Global survey of aftershock area expansion patterns, *Phys. Earth planet. Int.*, **40**, 77–134.

Tolstoy, I. & Ewing, M., 1950. The T-phase of the shallow-focus earthquake, *Bull. seism. Soc. Am.*, **40**, 25–51.

Wetzel, L.R., Wiens, D.A. & Kleinrock, M.C., 1993. Evidence from earthquakes for bookshelf faulting at large non-transform ridge offsets, *Nature*, **362**, 235–237.

Yang, Y. & Forsyth, D.W., 2003. Improving epicentral and magnitude estimation of earthquakes from T phases by considering the excitation function, *Bull. seism. Soc. Am.*, **93**(5), 2106–2122.